(article starts on next page)

Mitigation of interfacial dielectric loss in aluminum-on-silicon superconducting qubits

Check for updates

Janka Biznárová [1] ✉, Amr Osman [1], Emil Rehnman [1], Lert Chayanun[1], Christian Križan [1], Per Malmberg [2], Marcus Rommel[1], Christopher Warren [1], Per Delsing [1], August Yurgens[1], Jonas Bylander [1] ✉ & Anita Fadavi Roudsari [1] ✉

We demonstrate aluminum-on-silicon planar transmon qubits with time-averaged T_1 energy relaxation times of up to 270 μs, corresponding to Q = 5 million, and a highest observed value of 501 μs. Through materials analysis techniques and numerical simulations we investigate the dominant source of energy loss, and devise and demonstrate a strategy toward its mitigation. Growing aluminum films thicker than 300 nm reduces the presence of oxide, a known host of defects, near the substrate-metal interface, as confirmed by time-of-flight secondary ion mass spectrometry. A loss analysis of coplanar waveguide resonators shows that this results in a reduction of dielectric loss due to two-level system defects. The correlation between the enhanced performance of our devices and the film thickness is due to the aluminum growth in columnar structures of parallel grain boundaries: transmission electron microscopy shows larger grains in the thicker film, and consequently fewer grain boundaries containing oxide near the substrate-metal interface.

Limited qubit coherence is still one of the main challenges for developers of solid-state quantum computing hardware. In the gate model of quantum computation, errors per quantum gate well below a tenth of a percent are required to execute meaningful quantum algorithms—and the lower the errors, the less overhead is needed for error correction and error mitigation.

Superconducting qubits represent a leading platform for quantum computation. Their coherence time improvement, from nanoseconds at their conception to milliseconds today, is nothing less than remarkable[1–4]. Progress has been driven by discoveries and systematic engineering to identify and mitigate the sources of decoherence. This effort has two components: a reduction of the qubits' sensitivity to noise by development of innovative device design concepts[5–8] and a reduction of the noise itself by engineering the qubits' electromagnetic environment[8,9] and improved fabrication methods[10,11] informed by materials science[7,12,13].

Coplanar waveguide (CPW) resonators and transmon qubits[5,14] are commonly used for studying coherence and identifying loss mechanisms in superconducting devices. The dominating decoherence source within these devices is dielectric loss and noise, attributed to charged two-level-system (TLS) defects at surfaces and interfaces, i.e., in thin sheets at the substrate-metal (SM), metal-air (MA), and substrate-air (SA) interfaces[15–20]. Oxide-based defects are known contributors to TLS loss[21,22].

Among superconducting materials for qubits, aluminum (Al) has been a dominant material within the community: the ease and reproducibility of thin-film deposition, low cost, well-described chemistry, and the robust Josephson effect in small tunnel junctions comprised of aluminum oxide sandwiched between aluminum electrodes have made this material an attractive choice.

The achieved energy relaxation time (T_1) of transmon qubits in a planar geometry whose wiring layer is made of aluminum is currently about 100 μs[7]. However, recent years have seen an impressive improvement for transmon qubits with wiring layers made of tantalum, a less explored material for quantum devices, showing average T_1 in the range of 300–480 μs[23,24]. This progress has subsequently spread to the more traditionally used materials titanium nitride and niobium, with average T_1 up to 291 μs and 210 μs, respectively[25,26]. An apparent advantage of these materials over aluminum is their ability to withstand harsh chemical surface cleaning.

Here we demonstrate planar transmon qubits made of aluminum-on-silicon substrates, with time-averaged T_1 of up to 270 μs ($Q = \omega_q T_1 = 5$ million, where ω_q is the qubit frequency). The improvement is mirrored in CPW resonators' quality factor measurements: the Q factor's dependence on circulating power indicates that the increased relaxation time is due to a reduction of TLS losses. We achieve this improvement by depositing a thicker layer of aluminum—300 nm or more—compared to our previous

[1]Microtechnology and Nanoscience, Chalmers University of Technology, Gothenburg, Sweden. [2]Chemistry and Chemical Engineering, Chalmers University of Technology, Gothenburg, Sweden. ✉e-mail: jankab@chalmers.se; jonas.bylander@chalmers.se; fadavi@chalmers.se

standard of 150 nm. We conduct material depth profiling by time-of-flight secondary ion mass spectrometry (ToF-SIMS) and identify an aluminum-film-thickness dependence of the oxygen concentration at the SM interface, which decreases for thicker films. Further, we show by transmission-electron microscopy (TEM) that the thicker film has larger grains; we therefore interpret the reduced oxygen presence as being due to a smaller prevalence of grain boundaries in the thicker film and hence fewer sources of interfacial dielectric loss. Our numerical simulations of the loss participation due to the different dielectrics present in the device support this interpretation.

Results

Qubit coherence

We show a representative schematic of the transmon (Xmon[27]) qubit circuit in Fig. 1a. The device has a 2D architecture and consists of a Josephson junction shunted by a large capacitor, which is coupled to a quarter-wavelength ($\lambda/4$) CPW resonator. The CPW resonator is used for readout as well as qubit control. The devices are fabricated on silicon (Si) substrates and stripped of surface oxides prior to Al deposition. We present more details on device fabrication and measurement in the "Methods" section.

In Fig. 1b, we present coherence data of 40 out of the 42 measured qubits made with Al films of various thicknesses of 150 nm (previously our standard thickness), 300 nm, and 500 nm. Two qubits were disregarded from the analysis due to inconsistent measurement results, see Supplementary Note I. The figure shows a trend toward higher coherence times with thicker films. The average quality factor Q, plus/minus one standard deviation, is $2.1 \times 10^6 \pm 23\%$ for the qubits on the 150 nm thick film, and $3.3 \times 10^6 \pm 26\%$ for those on the thicker films.

The qubit frequencies range from 2.8 GHz to 5.0 GHz, while the resonator frequencies are between 6.0 GHz and 6.8 GHz, see Supplementary Table 1. For simplicity of device design and characterization, there is no Purcell filtering present in the device to mitigate spontaneous emission from the qubit into its resonator and the transmission line. Therefore, for these long-T_1 qubits, Purcell decay is non-negligible and needs to be included among the limiting factors of the qubits' lifetime

$$\frac{1}{Q} = \frac{1}{Q_{\text{TLS}}} + \frac{1}{Q_{\text{p}}} + \frac{1}{Q_{\text{qp}}} + \frac{1}{Q_{\text{rad}}} + \cdots \qquad (1)$$

Here Q_{TLS}, Q_{p}, Q_{qp}, and Q_{rad} are the theoretical quality factors attributed to TLS, Purcell decay, quasiparticles, and other radiation losses not related to Purcell decay, respectively.

The time constant of the Purcell decay for each qubit is calculated as $T_{\text{p}} = \gamma^{-1}$, with the decay rate γ[5],

$$\gamma = \kappa \frac{g^2}{\Delta^2}, \qquad (2)$$

where the cavity decay rate is $\kappa = \omega_{\text{r}}/Q_{\text{l}}$, the qubit-resonator coupling is $g = \sqrt{\chi\Delta}$, and the qubit-resonator detuning is $\Delta = \omega_{\text{q}} - \omega_{\text{r}}$. Here ω_{r} denotes the resonator frequency, Q_{l} represents the resonator's loaded (total) quality factor and χ is the dispersive frequency shift.

The qubit-resonator detunings vary between the devices due to variations in the Josephson junctions. Qubits with a smaller qubit-resonator detuning are more strongly Purcell-limited than others. As a result, a direct comparison between the qubits based solely on their T_1 is not the correct way of evaluating the qubits' performance.

To compare qubits of different frequencies while simultaneously taking the effect of the Purcell decay into account, we plot the qubits' quality factor Q as a function of T_1/T_{p} in Fig. 1b. We choose Q instead of T_1 since the latter depends directly on frequency, which also varies across devices. Now, rewriting Equation (1) while ignoring the loss due to quasiparticles and radiation, we are left with $(1/Q)(1 - T_1/T_{\text{p}}) = 1/Q_{\text{TLS}}$. The quality factor will therefore approach its limit set by the TLS loss when $T_1/T_{\text{p}} \ll 1$.

In Fig. 1b, the data shown in blue belong to qubits fabricated on a 150 nm thick wiring layer, while the purple and pink markers show qubits fabricated on 300 and 500 nm thick layers, respectively. While the average Q for the thicker films is higher, the separation between the datasets scales with the Purcell effect. When $T_1 \leq 0.5T_{\text{p}}$, a range at which the qubits are not significantly limited by Purcell decay, the data for the thicker and thinner films are clearly separated, with the qubits fabricated with the thinner film (150 nm) showing a lower quality factor compared with those on the thicker films ($\geq$300 nm). There is a subtle difference between the quality factors of the qubits on 300 and 500 nm films; however, the difference is not so pronounced as to clearly differentiate the qubits with these two film thicknesses. The average quality factor in this range is $2.1 \times 10^6 \pm 22\%$ for the qubits on the thin film, while it increases by 76% to $3.7 \times 10^6 \pm 18\%$ for those on the thicker films. For a more stringent case of $T_1 \leq 0.25T_{\text{p}}$, the average
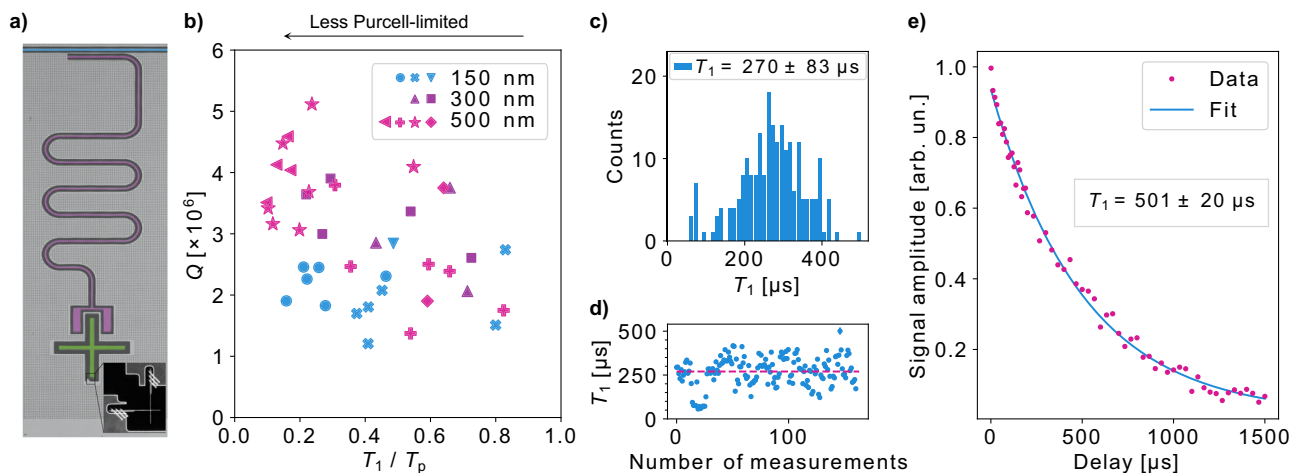
Fig. 1 | Qubit design and coherence data. a False-colored micrograph of a qubit device. A portion of the input/output transmission line is shown in blue, coupled to a readout resonator, shown in purple. The qubit capacitor is shown in green. The inset shows a scanning electron micrograph (SEM) of the Josephson junction. **b** Time-averaged qubit quality factor Q as a function of the measured qubit relaxation time relative to the calculated Purcell decay time, T_1/T_{p}, for qubits fabricated on wiring layers of 150, 300, and 500 nm. The quality factor of those qubits with $T_1 \ll T_{\text{p}}$ is closer to the limit set by the TLS loss. Qubits displayed by the same marker are made on one wafer. **c** A histogram showing the relaxation time of the best qubit with average $T_1 = 270$ μs plus/minus one standard deviation of 83 μs. **d** 160 T_1 measurements of the qubit in (**c**) over a span of 48 h. Fit error bars are smaller than markers where not visible. **e** Demonstration of the exponential fit to the longest T_1 measured.

quality factor becomes $3.9 \times 10^6 \pm 16\%$ for the thicker films. Assuming a typical qubit frequency of $\omega_q/2\pi = 3$ GHz, the corresponding relaxation time becomes ~200 μs for a qubit made from the thicker 300–500 nm films, in the weakly Purcell-limited regime.

We remark that the coherence times quoted in Fig. 1b are mean values gathered by measuring each qubit for at least 24 h. This is necessary to accurately assess a qubit's quality since the coherence time of superconducting qubits is known to fluctuate over time[9,12,22,28]. In Fig. 1c we show the histogram of the relaxation time of the best qubit, labeled Q27 in Supplementary Table 1. The histogram contains 160 averaged values (see Fig. 1d) obtained over a span of 48 h. We find an average relaxation time of 270 μs, on par with the numbers reported for the best qubits on titanium nitride and niobium films[25,26]. In Fig. 1e we present the longest measured relaxation time for the aforementioned qubit, together with its corresponding fit, showing $T_1 = 501$ μs.

The improvement of T_1 in the thicker films is also reflected in the values obtained for the spin echo decoherence time T_2^{echo}, as $T_2^{echo} > T_1$ for most of our qubits, see Supplementary Table 1. Although we find mean values as long as 307 μs, the spin echo decoherence time does not quite reach the theoretical maximum of $2T_1$, indicating that the coherence of our qubits is not solely limited by T_1, or by the type of dephasing noise typically canceled by the spin echo sequence.

Resonator loss

In order to distinguish and quantify the particular energy loss mechanisms at play, we also fabricate and measure 50 bare $\lambda/4$ CPW resonators with resonance frequencies in the range of 4–8 GHz. The center conductor width (w) and the gap to ground (g) are 20 μm and 10 μm, respectively, corresponding to near 50 Ω impedance. The internal quality factors Q_i of the resonators are extracted by fitting the transmission scattering parameter S_{21} vs. frequency using a resonance circle fitting method with diameter correction adapted directly from ref. 29.

For TLS-loss-limited resonators, Q_i at low drive powers will be diminished according to the model for interacting TLSs[30–32],

$$\frac{1}{Q_i} = F\delta_{TLS}^0 \frac{\tanh(\hbar\omega_r/2k_BT)}{(1 + \langle n \rangle/n_c)^\beta} + \delta_0, \quad (3)$$

where $F\delta_{TLS}^0$ describes the loss due to parasitic TLSs, with F quantifying the TLS filling (also known as the total TLS participation ratio), and δ_{TLS}^0 the TLS density. n_c is the critical photon number required to saturate a single TLS on average, and β describes how quickly the TLSs saturate with power. The temperature-dependent factor $\tanh(\hbar\omega_r/2k_BT)$ is ~1 in our temperature regime (T denotes the temperature, and $\hbar$ and k_B are the Planck and Boltzmann constants, respectively). The power-independent term δ_0 quantifies other sources of loss, such as resistive or radiative losses. The average number of photons circulating in the resonator $\langle n \rangle$ is estimated using ref. 33

$$\langle n \rangle = 2 \frac{Z_0}{Z_r} \frac{Q_l^2}{Q_c} \frac{P_{in}}{\hbar\omega_r^2}, \quad (4)$$

where Z_0 and Z_r are the characteristic impedances of the transmission line and the resonator, respectively, and P_{in} is the microwave power delivered to the input port of the device. Q_l and Q_c are the loaded and coupling quality factors, respectively.

In Fig. 2a, we compare the extracted Q_i of two resonators with the same resonance frequency ($\omega_r/2\pi = 4.45$ GHz) on 150 and 500 nm films. Both resonators show a similar Q_i when $\langle n \rangle \gtrsim 10^6$. However, the resonator fabricated on the 500 nm film has a higher internal quality factor at lower photon levels. We fit the quality factors to the TLS model of Equation (3) and obtain $F\delta_{TLS}^0$, presented in Fig. 2b for all of the resonators. For the resonators on the 500 nm film, $F\delta_{TLS}^0$ has settled at a lower level (5×10^{-7} on average) in comparison with those made with the 150 nm film (1×10^{-6} on average), indicating a reduction in the loss due to the TLSs. As for the
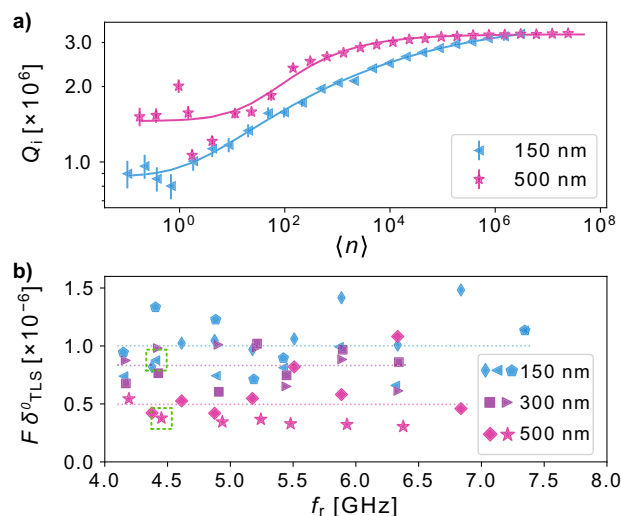
Fig. 2 | Study of energy loss in bare resonators. a Internal quality factor Q_i as a function of average number of photons $\langle n \rangle$ fitted to the TLS model in Equation (3), for two resonators with a resonant frequency of 4.45 GHz. **b** TLS loss $F\delta_{TLS}^0$ extracted from the TLS model fits, as a function of frequency for resonators of three different film thicknesses. Data indicated by the same marker belong to resonators on a single chip. The dashed lines indicate the average value of $F\delta_{TLS}$ for a given film thickness. For best visual comparability, the resonators showcased in (**a**) are chosen for their proximity in frequency and high-power Q_i, and are indicated in (**b**) with a dashed-line square.

resonators made with the 300 nm Al, $F\delta_{TLS}^0$ is in-between, with an average value of 8×10^{-7}.

From the fit we also obtain δ_0 in Equation (3), see Supplementary Fig. 1. Interestingly, we observe a frequency-dependent increase in the non-TLS related loss, δ_0, in the 500 nm thick films. We did not observe this increased loss in our qubits, whose frequencies lie below 5 GHz, where this loss seems to be less prominent. However, depending on its origin as well as its dependence on device geometry, this loss mechanism could become limiting for higher-frequency qubits fabricated on thicker films. We present a further investigation of this loss in Supplementary Note II.
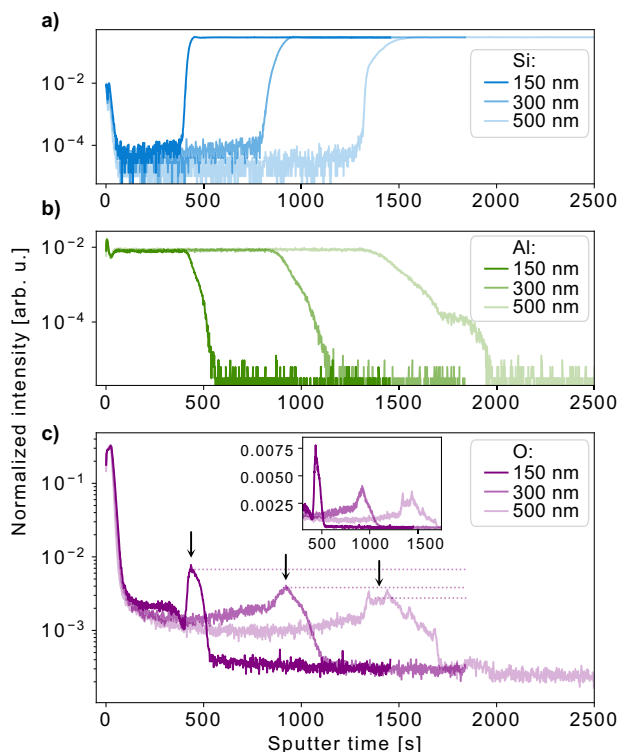
In the model for interacting TLSs, the parameter β describes how sharply the TLSs saturate with increased power. In our data, β is scattered, falling between 0.15 and 0.4 for most resonators (which is typically reported in studies[32]), with no discernible trend across the devices.

Materials analysis

The presence of parasitic TLS defects is mainly attributed to amorphous oxides at the materials interfaces[15,21], although their microscopic origin is debated. We therefore perform an elemental analysis of representative samples, focusing on oxygen (O) residing near the material interfaces. We perform this analysis using time-of-flight secondary ion mass spectrometry (ToF-SIMS), a highly accurate method capable of simultaneous analysis of species with different masses[34]. To obtain a depth profile of the species of interest across all interfaces, we use an auxiliary sputter beam. This method is further detailed in Supplementary Note III.

The samples under analysis are pieces of a Si wafer coated with Al films of the three different thicknesses representative of our devices (150, 300, and 500 nm). To discount wafer-to-wafer variation in substrate material properties, these three pieces originate from the same wafer. After the splitting of the wafer, the Si pieces underwent a cleaning and deposition procedure identical to that used during the qubit and resonator fabrication.

The intensity of the detected signal identifying Si, Al, and O across the thickness of the sample is plotted in Fig. 3, normalized to the total ion count. Each trace starts at the metal-air (MA) interface, then continues through the metal and ends inside the substrate.
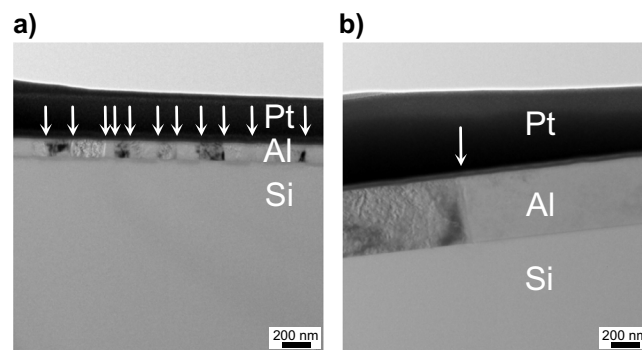
Fig. 4 | Investigation of the grain boundaries. TEM images showing the grains of **a** 150 nm and **b** 500 nm thick films. The grain size increases with film thickness, resulting in fewer grain boundaries. The arrows show the locations of the grain boundaries. The dark regions at the Al–Si interface are due to diffraction effects caused by slightly out-of-focus settings used to enhance the grain boundaries. The platinum (Pt) layer is added during sample preparation for TEM.

Fig. 3 | Elemental analysis of the Al/Si material stack by ToF-SIMS. Depth profiles of **a** Si, **b** Al, and **c** O. Each plot contains data on three samples with varying Al thickness. The sharp increase in the intensity of Si in (**a**), and the arrows in (**c**), mark the SM interface of each sample. The inset in (**c**) shows the O peaks at the SM interface on a linear scale.

In Fig. 3a, we detect Si at the MA interface, which is likely coming from ambient air. Sputtering away more material, the intensity of the Si signal is low inside the metal, then rises abruptly at the SM interface, and saturates inside the Si substrate. In Fig. 3b, the intensity of the Al signal is initially high at the MA interface and inside the Al film, then plummets to the detection limit once we reach the substrate. The kink in the depth profile of the 500 nm Al film is caused by bottom topographical effects in the crater, related to sputtering through the relatively thick layer, and it is known that this can vary over the film's area. Supplementary Fig. 4b contains the depth profile data of the same sample with measurements performed on a different place on the film, and there, no kink is observed in the Al signal.

In Fig. 3c, the intensity of the O signal starts high at the aluminum oxide-passivated MA surface, then stabilizes at a lower level inside the film. Sputtering further, there is a peak in the O intensity at the SM interface, after which the trace levels out inside the Si substrate.

The diffusion constant of oxygen in aluminum is low at room temperature[35]; however, diffusion along grain boundaries is substantially faster[36]. Oxygen can exist in aluminum along the grain boundaries, as the evaporated Al grows in a high vacuum with a tendency to follow a columnar growth structure[37]. This observation emphasizes that lossy oxides exist not only at the direct interfaces but also within the grainy metal films, contributing to dielectric loss when in the vicinity of the interfaces.

We suggest that the peak at the SM originates from both the continuation of oxide along the grains, as well as from an interfacial oxide. The origin of this interfacial oxide could be a result of local, incomplete silicon oxide removal, or oxide regrowth after removal during transfer to the evaporator or while inside, resulting from residual oxygen content of the evaporation chamber. In Supplementary Note III we show that the oxygen is mainly present in the form of aluminum oxide, which is consistent with the thermodynamically favorable reduction of silicon oxides into aluminum oxides[38,39].

Comparing the three films in Fig. 3c, we find that the oxygen level inside the film decreases in the thicker films. The peak intensity is also lower in the thicker films, as indicated by the dashed lines.

While it appears in the data as if the Si/Al interface were broadening with increasing film thickness, this is unlikely to be a real feature of the samples. Instead, this broadening is a known artifact caused by surface roughening and atomic mixing during the sputter-assisted depth profiling[40,41]. Although disregarding the width of the peaks in similar scenarios is not unusual, we compare both the peak intensity and the integrated intensity for O across the entire Al film. We find a similar trend in both cases, that the intensity of the oxygen signal is strongest for the thinnest film. At the SM interface, the O intensity peak level scales with the ratio of 5:3:2 for 150 nm, 300 nm, and 500 nm films, respectively. The integrated intensity for O across the entire Al film, including the MA and SM interfaces, divided by film thickness scales with a ratio of 6:3:2.

When a film grows under a high vacuum, there are fewer impurities on the crystal faces that could change the energy of the crystal face or block the migration along the grain boundaries. As a result, the pure grain boundaries are mobile, and over time during the film growth, grain boundary motion takes place to minimize the surface and interface energies. Therefore, increasing a film's thickness (increased time) has a direct effect on the resulting grain size[37,42–44], which we confirm using transmission-electron microscopy (TEM). In Fig. 4, we observe long vertical grain boundaries that stretch uninterrupted all the way from the top surface to the interface with the Si substrate. The grain size increases with film thickness, which strongly impacts the morphology of the material interfaces. A larger grain size also provides fewer grain boundaries to trap residual oxygen during deposition, as well as to act as diffusion channels upon contact with the ambient atmosphere. While the electric field well inside the superconducting film is low, and therefore grain boundaries inside the film are unlikely to lead to additional loss, fewer grain boundaries acting as hosts of TLS in the vicinity of the SM interface can decrease the dielectric loss of this interface. Since the contribution of the SM interface to the overall loss is substantial (see the "Participation ratio simulations" section), a small change in the concentration of potential TLS defects has a significant impact on the total loss in the circuit.

At the MA interface, the oxygen contribution from the surface oxide is considerably greater than the oxide along the grain boundaries. As such, we do not observe a tangible effect in the reduction of oxygen presence between the samples with different densities of grain boundaries. The measurement traces identifying oxygen species at the surface of the three different film thicknesses are indistinguishable. Altering the thickness of a thin film can affect the MA interface as well, by way of changing the roughness of the
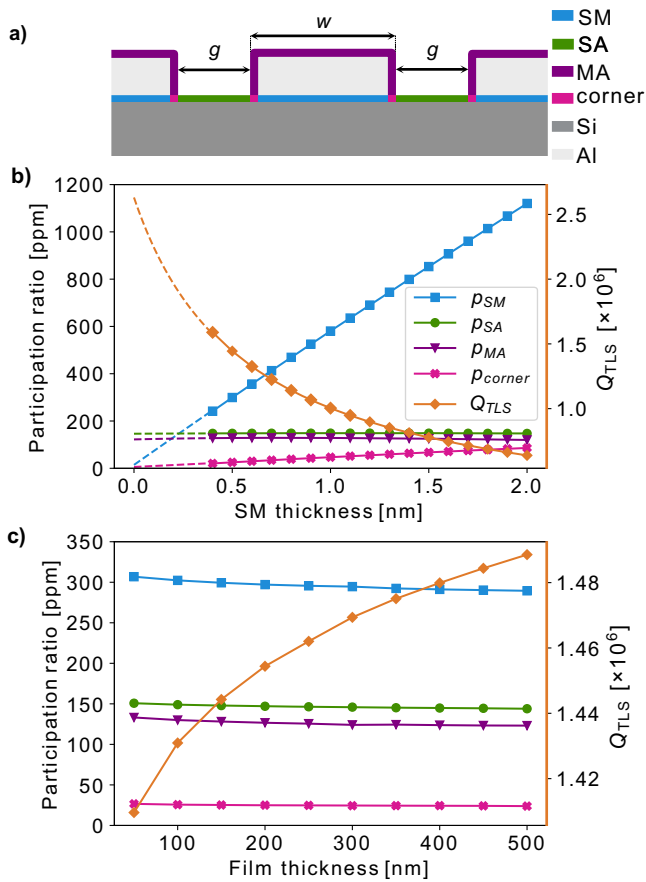
Fig. 5 | CPW geometry and participation ratio simulations. a CPW cross-section indicating the modeled interfaces. **b** 2D simulation results of a CPW resonator showing the variations in the participation ratio at different interfaces as a function of the dielectric thickness at the substrate-metal (SM) interface. The thickness of the metallic film is kept fixed at 150 nm. **c** Variation in the participation ratios as a function of the thickness of the metallic film of the CPW resonator. In both (**b**) and (**c**), the corresponding theoretical internal quality factor due to TLS loss is shown in orange (right axis). Note that although the majority share of the electric field is stored in the substrate (91–92%) and in air (8–9%), their corresponding participation ratios are not shown in the figure; these two media are not as lossy as the other interfaces (Table 1), and they do not hold a major part of the total loss.

Table 1 | Parameters used for participation ratio simulations in Fig. 5

Interface	$\tan\delta$	ϵ_r	Thickness Fig. 5b	Thickness Fig. 5c
Al	-	-	150 nm	50–500 nm
Air	0	1.0	2 mm	2 mm
Si	10^{-7}	11.7	280 µm	280 µm
MA	10^{-3}	7.0	5 nm	5 nm
SA	10^{-3}	4.0	2 nm	2 nm
SM	10^{-3}	4.0	0.4–2 nm	0.5 nm
corner	10^{-3}	4.0		

Note: For simplicity, the air environment (cryogenic vacuum) is assumed lossless and the values of $\tan\delta$ for SM, SA, and MA interfaces are considered equal. $\tan\delta = 10^{-3}$ stands at the lower bound of the limits reported by Wang et al.[46]. The CPW dimensions are $w = 20\,\mu m$ and $g = 10\,\mu m$.

the participation ratio weighted by the loss tangent of the material

$$1/Q_{\text{TLS}} = \sum_i p_i \tan\delta_i, \tag{5}$$

where p_i and $\tan\delta_i$ denote the participation ratio and the loss tangent at interface i, respectively (i: Si, MA, SA, SM, and corner). The various interfaces are illustrated in Fig. 5a.

The energy participation ratio at the MA and SA interfaces changes negligibly by varying the dielectric thickness at the SM. However, at the SM interface (and the corresponding corners), there is a linear dependence of the field concentration on the SM dielectric thickness. Moreover, compared to the MA and SA interfaces, a considerable fraction of the electric field resides at the SM interface. With the removal of the silicon native oxide prior to metal deposition, the *effective* dielectric thickness at the SM interface is estimated to be about 0.5 nm[47]. The resulting participation ratio, and the corresponding loss, assuming equal loss tangents, is about twice those at the MA and SA interfaces. Reducing the SM dielectric to about 0.25 nm decreases the corresponding SM loss, yielding an almost equal value of the participation ratio by the three interfaces. Below this level, the loss is dominated by the MA and SA interfaces.

We ran a second round of simulations to explore the evolution of participation ratios if the thickness of the metallic layer is varied. The presented results in Fig. 5c show only a slight variation in the participation ratios, as well as in the quality factor of the resonator. From the simulations above and the materials analysis in the "Materials analysis" section, we conclude that the better performance of the devices with the thicker metallic layers is due to the reduction of the dielectric loss at the SM interface, by way of reducing the number of grain boundaries.

Discussion

We observe a significant improvement in the energy relaxation time of transmon qubits on silicon substrates when fabricated using aluminum films thicker than 300 nm, whereas the previous standard in our laboratory, and generally in the field, has been thinner. This observation is based on measurements of 40 qubits and 50 resonators. We demonstrate transmon qubits with average relaxation times exceeding 200 µs on 500 nm films, with the best qubit showing a time-averaged $T_1 = 270\,\mu s$, corresponding to $Q = 5.1 \times 10^6$.

Despite removing the native oxide of the silicon substrate prior to Al deposition, we detect a presence of oxygen and aluminum oxide at the Al–Si interface, which, due to the relatively strong electric field at this interface, contributes to dielectric loss. Material-depth characterization by ToF-SIMS reveals a weakening intensity of the oxygen-signal peak at the substrate-metal interface with increasing film thickness from 150 to 300 to 500 nm.

We attribute the lower intensity of oxygen at the SM interface of thicker films, hence their lower dielectric loss, to the increased grain size in the
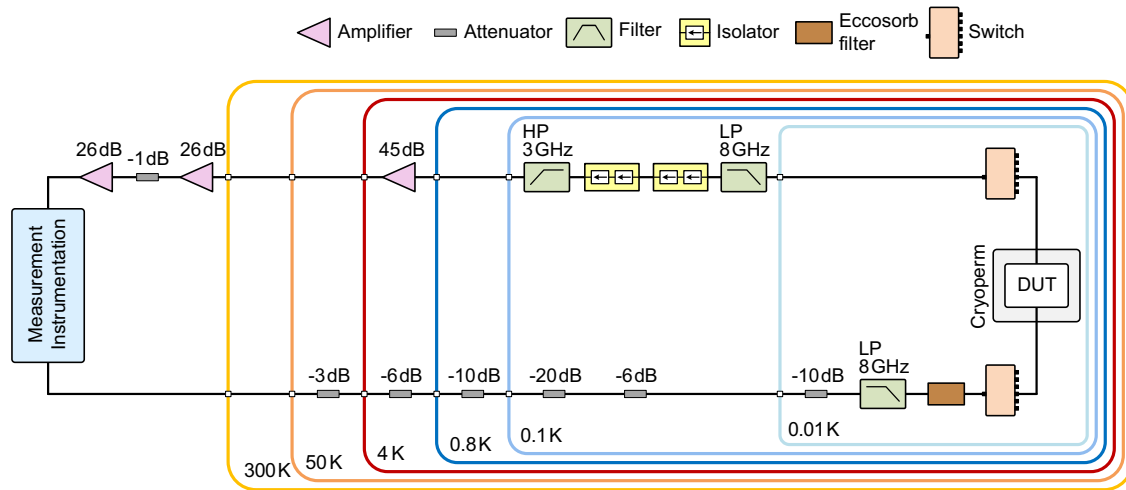
film's top surface. We perform an atomic force microscopy (AFM) to evaluate the surface roughness of a 150 nm and a 500 nm film, obtaining root mean square roughness R_q values of 5.9 nm and 6.3 nm, respectively, over a $5 \times 5\,\mu m^2$ area (Supplementary Fig. 5 in Supplementary Materials). This negligible difference, in conjunction with no observed change in MA oxide in the SIMS measurement, further discounts this interface from explaining the coherence measurement data.

Participation ratio simulations

In this section, we present energy participation ratio simulations of a 2D CPW geometry, showing that the reduced loss at the SM interface is the most likely reason for the improved quality factors of the devices made with thicker aluminum films. We also investigate if and when the loss due to other interfaces becomes dominant.

The cross-section of the simulated device is illustrated in Fig. 5a, with $w = 20\,\mu m$ and $g = 10\,\mu m$. Using the material parameters in Table 1[45,46], we first sweep the thickness of the dielectric at the SM interface and obtain the participation ratios presented in Fig. 5b. The data points show the simulation results from 2 nm down to 0.4 nm, while the lines represent polynomial fits to estimate the participation ratios for a thinner dielectric. The total loss due to TLSs, i.e., $1/Q_{\text{TLS}}$ – with Q_{TLS} presented in Fig. 5b as well – scales with

Fig. 6 | Cryogenic measurement setup.

thicker film, which we confirm in a TEM analysis. This consequently reduces the prevalence of oxidized grain boundaries in the vicinity of the interface, leading to lower loss.

From a study of loss in CPW resonators, we conclude that the contribution from TLS defects decreases for the thicker films and becomes comparable to loss due to other mechanisms. Whether growing even thicker films—or indeed using epitaxial films—can deliver qubits of superior performance demands further investigations. Our experiments and simulations point toward two obstacles: Firstly, a frequency-dependent loss appears for the thickest film of 500 nm. Secondly, with the reduced dielectric thickness at the SM interface (below about 0.2 nm), the corresponding interfacial loss falls below that of the other interfaces, with a lower impact on the total loss.

Methods
Device design and fabrication
In Fig. 1 we show a representative qubit design. It consists of a Josephson junction shunted by a large cross-type capacitor, which is coupled capacitively to the open end of a quarter-wavelength ($\lambda/4$) CPW resonator. This resonator is in turn inductively coupled via the shorted end to the input/output transmission line.

For readout resonators, both the center conductor width w and the gap g to the ground are 12 μm, while for the qubit capacitor $w = g = 24$ μm. The device structures are surrounded by an array of flux-trapping holes[48]. These are squares with a 2 μm long side, and a 10 μm pitch. The bare resonators used for energy loss quantification are also of the $\lambda/4$ CPW type, with $w = 2g = 20$ μm, coupled capacitively to the transmission line.

The devices are fabricated on high-resistivity ($\rho \geq 10$ kΩcm) intrinsic silicon substrates. The substrates are stripped of their native oxide in a 2% aqueous solution of HF and subsequently rinsed with deionized water to leave the Si surface terminated with a hydrogen monolayer[49].

Immediately after rinsing, we load the Si wafer into the load-lock of a Plassys MEB 550s evaporator, where it is heated to 300 °C for 10 min and then left to cool down to room temperature. This is done to desorb impurities and moisture from the surface of the wafer and to allow the evaporator to reach a satisfactory vacuum level of $\sim 3 \times 10^{-8}$ mbar in the evaporation chamber. We deposit the aluminum films at the rate of 1 nm s^{-1}, and then oxidize the top surface in situ in the load-lock without breaking the vacuum, in a static oxidation step. There is no crucible liner in the evaporation tool; the Al is melted directly in the water-cooled copper pocket. A summary of the films DC transport measurements is presented in Supplementary Note IV.

We then define all circuitry barring the Josephson junctions (JJs) in an optical lithography step. This includes the transmission line, the CPW resonators, qubit capacitors, and flux-trapping holes. We use a

resist stack of an e-beam resist, PMMA A2, and an optically sensitive resist such as S1805. The PMMA layer underneath the optical resist serves to protect the underlying Al from damage induced by the TMAH present in the photo-developer (MF319), which enables re-patterning. After successful patterning, the PMMA is ashed away in oxygen plasma. The pattern defined in the resist stack is then transferred into the Al layer via wet etching in a mixture of phosphoric, nitric, and acetic acids (aluminum etchant type A).

For qubit devices, JJs are fabricated using the patch-integrated cross-type technique adapted from ref. 50. The JJ electrodes pattern is transferred to the MMA EL12 + PMMA A6 resist stack using e-beam lithography (EBL), followed by deposition of the electrodes' metal in the Plassys evaporator using shadow evaporation and planetary turn. We evaporate 50 nm, 110 nm, and up to 300 nm of Al for the bottom and top electrodes and the patch layer, respectively. A liftoff in heated Remover 1165, followed by acetone and IPA cleaning completes the fabrication[51]. The optical resist is also removed by the same solvent cleaning sequence.

Measurement setup
We perform all of the microwave measurements at ~10 mK. The devices under test are placed in a light-tight copper sample box, mounted on a copper tail attached to the mixing chamber stage of a Bluefors LD250 dilution refrigerator. The copper tail is enclosed by a copper can coated with a layer of Stycast mixed with carbon and silicon carbide on the inside, which is in turn enclosed by a Cryoperm magnetic shield.

In Fig. 6 we show the cryogenic measurement setup with all components including attenuators, filters, microwave switches, isolators, and amplifiers. The input line attenuation is determined from an ac-Stark shift measurement[33,52].

As for the room temperature instrumentation, all resonator spectroscopy measurements necessary for the Q factor extraction are performed using an R&S ZNB8 vector network analyzer (VNA). When necessary, additional attenuation up to -20 dB is placed at the VNA output, in order to reach powers equivalent to a single photon circulating in the resonators.

The qubits are characterized using two alternative measurement setups. One setup consists of a multi-frequency lock-in amplifier platform (Intermodulation Products Presto-16), where both the pulses necessary to control the qubit and read out its resonator are synthesized directly on an FPGA. The measured signal is also digitized on this FPGA. The alternative qubit measurement setup consists of high-frequency signal generators (R&S SGS100a) and arbitrary waveform generators (Keysight PXIe M3202A 1GS/s AWG), whose outputs are upconverted with the help of IQ mixers to generate the desired high-frequency pulses. The detected signal is digitized using a Keysight PXIe M3102A 500 MS/s digitizer. Both setups have been verified to yield identical coherence results.

Data availability

References

1. Nakamura, Y., Pashkin, Y. A. & Tsai, J. S. Coherent control of macroscopic quantum states in a single-Cooper-pair box. *Nature* **398**, 786–788 (1999).
2. Houck, A. A. et al. Controlling the spontaneous emission of a superconducting transmon qubit. *Phys. Rev. Lett.* **101**, 080502 (2008).
3. Kjaergaard, M. et al. Superconducting qubits: current state of play. *Annu. Rev. Condens. Matter Phys.* **11**, 369–395 (2020).
4. Somoroff, A. et al. Millisecond coherence in a superconducting qubit. *Phys. Rev. Lett.* **130**, 267001 (2023).
5. Koch, J. et al. Charge-insensitive qubit design derived from the Cooper pair box. *Phys. Rev. A* **76**, 042319 (2007).
6. Sage, J. M., Bolkhovsky, V., Oliver, W. D., Turek, B. & Welander, P. B. Study of loss in superconducting coplanar waveguide resonators. *J. Appl. Phys.* **109**, 063915 (2011).
7. Dunsworth, A. et al. Characterization and reduction of capacitive loss induced by sub-micron josephson junction fabrication in superconducting qubits. *Appl. Phys. Lett.* **111**, 022601 (2017).
8. Gordon, R. T. et al. Environmental radiation impact on lifetimes and quasiparticle tunneling rates of fixed-frequency transmon qubits. *Appl. Phys. Lett.* **120**, 074002 (2022).
9. Burnett, J. J. et al. Decoherence benchmarking of superconducting qubits. *npj Quantum Inf.* **5**, 54 (2019).
10. Megrant, A. et al. Planar superconducting resonators with internal quality factors above one million. *Appl. Phys. Lett.* **100**, 113510 (2012).
11. Nersisyan, A. et al. Manufacturing low dissipation superconducting quantum processors. In *2019 IEEE International Electron Devices Meeting (IEDM)* 31.1.1–31.1.4 https://doi.org/10.1109/IEDM19573.2019.8993458 (2019).
12. Chang, J. B. et al. Improved superconducting qubit coherence using titanium nitride. *Appl. Phys. Lett.* **103**, 012602 (2013).
13. Murray, C. E. Material matters in superconducting qubits. *Mater. Sci. Eng. R Rep.* **146**, 100646 (2021).
14. Schreier, J. A. et al. Suppressing charge noise decoherence in superconducting charge qubits. *Phys. Rev. B* **77**, 180502 (2008).
15. Martinis, J. M. et al. Decoherence in Josephson qubits from dielectric loss. *Phys. Rev. Lett.* **95**, 210503 (2005).
16. Macha, P. et al. Losses in coplanar waveguide resonators at millikelvin temperatures. *Appl. Phys. Lett.* **96**, 062503 (2010).
17. Lisenfeld, J. et al. Electric field spectroscopy of material defects in transmon qubits. *npj Quantum Inf.* **5**, 105 (2019).
18. Molina-Ruiz, M. et al. Origin of mechanical and dielectric losses from two-level systems in amorphous silicon. *Phys. Rev. Mater.* **5**, 035601 (2021).
19. Niepce, D., Burnett, J. J., Kudra, M., Cole, J. H. & Bylander, J. Stability of superconducting resonators: Motional narrowing and the role of Landau-Zener driving of two-level defects. *Sci. Adv.* **7**, eabh0462 (2021).
20. Osman, A. et al. Mitigation of frequency collisions in superconducting quantum processors. *Phys. Rev. Res.* **5**, 043001 (2023).
21. Lisenfeld, J. et al. Observation of directly interacting coherent two-level systems in an amorphous material. *Nat. Commun.* **6**, 6182 (2015).
22. Müller, C., Lisenfeld, J., Shnirman, A. & Poletto, S. Interacting two-level defects as sources of fluctuating high-frequency noise in superconducting circuits. *Phys. Rev. B* **92**, 035442 (2015).
23. Place, A. P. M. et al. New material platform for superconducting transmon qubits with coherence times exceeding 0.3 milliseconds. *Nat. Commun.* **12**, 1–6 (2021).
24. Wang, C. et al. Towards practical quantum computers: transmon qubit with a lifetime approaching 0.5 milliseconds. *npj Quantum Inf.* **8**, 1–6 (2022).
25. Deng, H. et al. Titanium nitride film on sapphire substrate with low dielectric loss for superconducting qubits. *Phys. Rev. Appl.* **19**, 024013 (2023).
26. Kono, S. et al. Mechanically induced correlated errors on superconducting qubits with relaxation times exceeding 0.4 milliseconds. *Nat. Commun.* **15**, 1–12 (2024).
27. Barends, R. et al. Coherent Josephson qubit suitable for scalable quantum integrated circuits. *Phys. Rev. Lett.* **111**, 080502 (2013).
28. Schlör, S. et al. Correlating decoherence in transmon qubits: low frequency noise by single fluctuators. *Phys. Rev. Lett.* **123**, 190502 (2019).
29. Probst, S., Song, F. B., Bushev, P. A., Ustinov, A. V. & Weides, M. Efficient and robust analysis of complex scattering data under noise in microwave resonators. *Rev. Sci. Instrum.* **86**, 024706 (2015).
30. Gao, J. *The Physics of Superconducting Microwave Resonators*, Ph.D. thesis, California Institute of Technology (2008).
31. Pappas, D. P., Vissers, M. R., Wisbey, D. S., Kline, J. S. & Gao, J. Two level system loss in superconducting microwave resonators. *IEEE Trans. Appl. Supercond.* **21**, 871–874 (2011).
32. Burnett, J., Sagar, J., Kennedy, O. W., Warburton, P. A. & Fenton, J. C. Low-loss superconducting nanowire circuits using a neon focused ion beam. *Phys. Rev. Appl.* **8**, 014039 (2017).
33. Bruno, A. et al. Reducing intrinsic loss in superconducting resonators by surface treatment and deep etching of silicon substrates. *Phys. Rev. Lett.* **65**, 182601 (2015).
34. Benninghoven, A. Chemical analysis of inorganic and organic surfaces and thin films by static time-of-flight secondary ion mass spectrometry (TOF-SIMS). *Angew. Chem. Int. Ed. Engl.* **33**, 1023–1043 (1994).
35. Ross, A. J., Fang, H. Z., Shang, S. L., Lindwall, G. & Liu, Z. K. A curved pathway for oxygen interstitial diffusion in aluminum. *Comput. Mater. Sci.* **140**, 47–54 (2017).
36. Jaseliunaite, J. & Galdikas, A. Kinetic modeling of grain boundary diffusion: the influence of grain size and surface processes. *Materials* **13**, 1051 (2020).
37. Adamik, M., Barna, P. B. & Tomov, I. Columnar structures in polycrystalline thin films developed by competitive growth. *Thin Solid Films* **317**, 64–68 (1998).
38. Dadabhai, F., Gaspari, F., Zukotynski, S. & Bland, C. Reduction of silicon dioxide by aluminum in metal–oxide–semiconductor structures. *J. Appl. Phys.* **80**, 6505–6509 (1996).
39. Goodnick, S. M., Fathipour, M., Ellsworth, D. L. & Wilmsen, C. W. Effects of a thin SiO_2 layer on the formation of metal–silicon contacts. *J. Vac. Sci. Technol.* **18**, 949–954 (1981).
40. Yan, X. L., Duvenhage, M. M., Wang, J. Y., Swart, H. C. & Terblans, J. J. Evaluation of sputtering induced surface roughness development of Ni/Cu multilayers thin films by Time-of-Flight Secondary Ion Mass Spectrometry depth profiling with different energies O2+ ion bombardment. *Thin Solid Films* **669**, 188–197 (2019).
41. Gorbenko, V. et al. SIMS depth profiling and topography studies of repetitive III-V trenches under low energy oxygen ion beam sputtering. *J. Vac. Sci. Technol. B* **34**, 03H131 (2016).
42. Chaverri, D., Saenz, A. & Castano, V. Grain size and electrical resistivity measurements on aluminum polycrystalline thin films. *Mater. Lett.* **12**, 344–348 (1991).
43. Nik, S. et al. Correlation between Al grain size, grain boundary grooves and local variations in oxide barrier thickness of Al/AlOx/Al tunnel junctions by transmission electron microscopy. *SpringerPlus* **5**, 1–7 (2016).

44. Lita, A. E. & Sanchez, J. E. Effects of grain growth on dynamic surface scaling during the deposition of al polycrystalline thin films. *Phys. Rev. B* **61**, 7692–7699 (2000).
45. Martinis, J. M. and Megrant, A. UCSB final report for the CSQ program: review of decoherence and materials physics for superconducting qubits. Preprint at https://arxiv.org/abs/1410.5793 (2014).
46. Wang, C. et al. Surface participation and dielectric loss in superconducting qubits. *Appl. Phys. Lett.* **107**, 162601 (2015).
47. Kosen, S. et al. Building blocks of a flip-chip integrated superconducting quantum processor. *Quantum Sci. Technol.* **7**, 035018 (2022).
48. Chiaro, B. et al. Dielectric surface loss in superconducting resonators with flux-trapping holes. *Supercond. Sci. Technol.* **29**, 104006 (2016).
49. Trucks, G. W., Raghavachari, K., Higashi, G. S. & Chabal, Y. J. Mechanism of hf etching of silicon surfaces: a theoretical understanding of hydrogen passivation. *Appl. Phys. Lett.* **106**, 504–507 (1990).
50. Osman, A. et al. Simplified Josephson-junction fabrication process for reproducibly high-performance superconducting qubits. *Appl. Phys. Lett.* **118**, 064002 (2021).
51. Remover 1165, https://kayakuam.com/wp-content/uploads/2019/09/Remover-1165-Data-Sheet-RH.pdf (2019), accessed 31 January 2024.
52. Macklin, C. S. *Quantum Feedback and Traveling-wave Parametric Amplification in Superconducting Circuits*, Ph.D. thesis, UC Berkeley (2015).

Author contributions
Conceptualization: Janka B., A.F.R., and Jonas B. Fabrication and microwave measurements: Janka B., A.O., E.R., and L.C. with input from M.R. and A.F.R. (fabrication) and C.W. and C.K (measurements) SIMS measurements: P.M. Data analysis: Janka B., A.O., E.R., L.C., A.F.R., A.Y., Jonas B., P.M., and P.D. Funding acquisition: Jonas B. and P.D. Supervision: A.F.R., Jonas B., and A.Y. Writing – original draft & editing: Janka B., A.F.R., and Jonas B. Writing – review: all authors.

Competing interests
The authors declare no competing interests.

Additional information
Supplementary information The online version contains supplementary material available at https://doi.org/10.1038/s41534-024-00868-z.

Correspondence and requests for materials should be addressed to Janka Biznárová, Jonas Bylander or Anita Fadavi Roudsari.

Reprints and permissions information is available at http://www.nature.com/reprints

Publisher's note Springer Nature remains neutral with regard to jurisdictional claims in published maps and institutional affiliations.